Iraqi Journal of Science, 2025, Vol. 66, No. 12, pp: 5789- 5804
DOI: 10.24996/ijs.2025.66.12.41

ISSN: 0067-2904

Computation of Some Families of Frozen Orbits in the Field of Triaxial Moon

O.M.Ramla*, F.A.Abd El-Salam, W.A.Rahoma, E.H.Kattab
Astronomy space science and Meteorology Department, Faculty of science, Cairo University, Cairo, Egypt.

Received: 13/6/2024 Accepted: 15/12/2024 Published: 30/12/2025

Abstract

In this study, families of frozen orbits for a satellite revolving around the triaxial Moon are investigated. The Hamiltonian for this scenario is formulated, taking into account the lunar gravitational zonal harmonic coefficients up to J_6 along with its most effective triaxiality factors, namely J_{22}, J_{31}, J_{32} and J_{33}. Using canonical Lie transforms, the Hamiltonian undergoes an average process where short-term periodic elements are eliminated while retaining secular components up to the second order. New families of critical inclination roots are obtained; one of the roots lies in the vicinity of polar orbits, and the other is close to typical critical inclinations. This research investigates how variations in eccentricity, semi-major axis, and argument of periapsis affect these critical inclinations. A family of frozen orbits around the apsidal line and their graphical representation are revealed. To ensure such orbits, the argument of periapsis is solved. This establishes certain constraints when selecting the inclination that meets the criteria for the frozen argument of periapsis orbits. Significant perturbations in the critical inclination occur in high lunar orbits.

Keywords: Lunar orbiters; Frozen orbits; Critical inclination; Triaxial Moon; Gravitational perturbations

1. Introduction

The frozen orbit is an orbit in which the long-term changes in the argument of periapsis (ω) and eccentricity (e) are minimal or negligible. More precisely, it is characterized by nearly constant inclination (I), semi-major axis (a), and eccentricity (e), with minimal variations in the argument of periapsis (ω). Based on Earth's dynamical parameters; $J_n, n = 2,3$, the frozen orbits are treated, see Weilian [1]. He utilized Brouwer's results for this purpose [2]. Even though the restrictions on frozen orbits are not overly strict, they require a very low eccentricity near the circular orbits. Considering only the second order of zonal harmonics J_2, the frozen orbits exhibit the expected critical inclinations (i.e., $63.4°$ or $116.6°$). By investigating the temporal variations of ω and I elements up to the term $\mathcal{O}(J_2)$, it reveals that $d\omega/dt \to 0$ nearby $I_c \cong 63.4$, indicating I_c for critical inclination. Thus, nearby I_c the long-period behaviour of ω shows a libration with a minimal period of $2\pi/k \simeq 102$ years, typically a period of order$J_2^{-3/2}$and approaching ∞ as$e \to 0$. The corresponding motion$I$exhibits an amplitude of order$J_2^{1/2}$ (providing e is non-zero). Analogous logic applies for e. was away fromI_c, the argument of periapsis ω propagates with a period within order of J_2^{-1}, hence the motion amplitudes in e and $I$are of orderJ_2. One can find that the

perturbations in e and I are noticeably greater than elsewhere by a factor$J_2^{-1/2} \cong 30$nearI_c. Adding J_4,the coefficient J_2^3 becomes$J_2(J_4 + J_2^2)$, since $(J_4 + J_2^2) < 0$, leading to stability in the equilibrium position at $\pm\pi/2$. Numerous studies introduced critical inclination, with a notable contribution, that is worth to sketch. Hori [3] and Garfinkel [4], used the Von Zeipel technique and Bohlin procedure to obtain solutions taking into accountJ_2 and J_4up to $J_2^{1/2}$in terms of elliptic integrals. Izsak [5] considered the qualitative behaviour of the phase plane considering J_2 and J_4. Aoki [6], Hoots and Fitzpatrick [7] reviewed the phase plane behaviour from small to moderate eccentricities with the unsatisfactory assumption $J_n \equiv \mathcal{O}(n)$, Delhaise and Henrard [8], Henrard [9], Delhase and Morbidelli [10] and Delsate, et al. [11]. Based on these studies, many ideas have been developed on the lunar frozen orbits, according to Park and Junkins [12]. To obtain low-altitude frozen orbits around planetary satellites, Scheeres, et al. [13], San-Juan et al. [14], and Paskowitz and Scheeres [15] considered the perturbation due to the first zonal harmonics. Further details on the problem and related issues can be found by referring to Lara et al. [16, 17, 18], Tzirti et al. [19, 20], Liu et al. [21, 22], Carvalho, et al. and [23, 24], Ulivieri, et al. [25], Pardal, et al. [26] and Rahoma, et al. [27, 28]. In the three body problem, the frozen orbits concept can be utilized in designing orbits for particular missions, see Zotos [29]. Additionally, it can be expanded to orbits featuring resonant capture, Haberman, et al. and Quinn, et al. [30, 31]. Abd El-Salam, et al. [32] computed the effects of the post-Newtonian on the critical inclination problem within the artificial satellite theory, considering the first zonal harmonic of the geopotential J_2 as a small parameter of order one. Abd El-Salam and Ahmed [33] obtained a canonical solution of the critical inclination problem taking into account PN-corrections using the Bohlin technique. Khattab, et al. [34] constructed frozen orbits for a lunar solar sail. Sirwah, et al. [35] studied the moderate altitude frozen orbits around the Moon, taking into account the first seven zonal harmonics of the lunar potential plus Earth as a third body perturbation. Finally, Abd El-Salam, et al. [36] computed frozen orbits around the apsidal line about the triaxial Moon considering the coupling quadrupole nonlinearity. Abd El-Salam, et al. [37] studied the frozen orbits of the charged satellites under zonal harmonic perturbations, considering the geopotential up to J_6 zonal harmonics.

Following this overview, this paper includes: Section two examines the Hamiltonian of a satellite keeping the terms up to J_6 in addition to the moon's triaxiality. Furthermore, the Hamiltonian is obtained in the Delaunay canonical set in section 3. While in section 4, the Hamiltonian is normalized by eliminating short-period terms like mean anomaly. Section 5 presents the construction of the canonical equations for the frozen argument of pericentre and eccentricity. In section 6, the previous canonical equations are solved for the inclination. In section 7, the graphical representations for the canonical equation are shown, with subsequent subsections and their analyses. In section 8, the conclusion is written.

2. The formulation of the Hamiltonian

Considering a Lunar orbiter of mass m orbiting a triaxial central body (in our study, the Moon will be considered as a central body), then the Hamiltonian, given by Lara, M. [38], can be written as follows:

$$\mathcal{H} = \frac{m^2}{2}(\dot{r} \cdot \dot{r}) - \frac{\mu}{r} - \mathcal{R}(r) \tag{1}$$

Where $r$is the satellite's radius vector relative to the Moon's center, r is the magnitude, $\dot{r}$ is the orbital velocity, and $\mu = 4.9048695 \times 10^{12} m^3\ \mathrm{s}^{-2}$is the Moon's gravitational parameter. The function $\mathcal{R}(r)$ denotes the perturbations under consideration. In this

model, J_2 represents the Moon's oblateness, including coefficients up to the sixth zonal harmonic, along with its effective triaxiality terms, specifically J_{22}, J_{31}, J_{32}, and J_{33}. In this representation, $\mathcal{R}(r)$ becomes,

$$\mathcal{R}(r) = \frac{\mu J_2 R_M^{\,2}}{4r^3}\left[(3S^2-2) - 3S^2\cos F_{2,2,0}\right] + \frac{\mu J_3 R_M^{\,3}}{8r^4}\left[(15S^3-12S)\sin F_{1,1,0} - 5S^3\sin F_{3,3,0}\right] + \frac{\mu J_4 R_M^{\,4}}{64r^5}\left[(24-120S^2+105S^4) + (120S^2-140S^4)\cos F_{2,2,0} + 35S^4\cos F_{4,4,0}\right] + \frac{\mu J_5 R_M^{\,5}}{128r^6}\left[(240S-840S^3+630S^5)\sin F_{1,1,0} + (280S^3-315S^5)\sin F_{3,3,0} + 63S^5\sin F_{5,5,0}\right] + \frac{\mu J_6 R_M^{\,6}}{512r^7}\left[(-160+1680S^2-3780S^4+2310S^6) + (-1680S^2 + 5040S^4 - 3465S^6)\cos F_{2,2,0} + (-1260S^4+1386S^6)\cos F_{4,4,0} - 231S^6\cos F_{6,6,0}\right] + \frac{3\mu J_{22} R_M^{\,2}}{4r^3}\left[2S^2\cos F_{0,0,2} + (1-C)^2\cos F_{2,2,-2} + (1+C)^2\cos F_{2,2,2}\right] + \frac{3\mu J_{31} R_M^{\,3}}{16r^4}\left[(-1-11C+5C^2+15C^3)\cos F_{1,1,1} + (-1+11C+5C^2-15C^3)\cos F_{1,1,-1} + 5(1+C-C^2-C^3)\cos F_{3,3,+1} + 5(1-C-C^2+C^3)\cos F_{3,3,-1}\right] + \frac{15\mu^5 R_M^{\,3} J_{32}}{16r^4}\left[(2-4C-7C^2+2C^3)\sin F_{1,1,2} + (2+4C-7C^2-3C^3)\sin F_{1,1,-2} + (2+4C+C^2-2C^3)\sin F_{3,3,2} + (2-4C+C^2+2C^3)\sin F_{3,3,-2}\right] + \frac{15\mu J_{33} R_M^{\,3}}{8r^4}\left[3(-1-C+C^2+C^3)\cos F_{1,1,3} + 3(-1+C+C^2-C^3)\cos F_{1,1,-3} + (-1-3C-3C^2-C^3)\cos F_{3,3,3} + (-1+3C-3C^2+C^3)\cos F_{3,3,-3}\right] \quad (2)$$

Where J_2 , J_3 , $J_4, J_5, and\ J_6$ are the coefficients of the zonal harmonics due to the asphericity of the Moon's gravity field. (a, I, ω, f) are some of the predefined Keplerian elements, R_M is the Moon's mean equatorial raduis. $C = cos\, I$, $S = sin\, I$, also adopting the notation $F_{i,j,k} = if + j\omega + k(\Omega - \lambda_m t)$, where t is the time and λ_m is the rotation rate of the Moon.

The adopted values of the included coefficients and the equatorial radius of the Moon are:

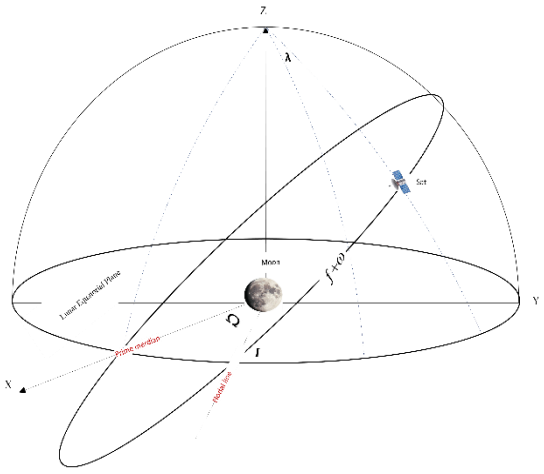

Figure. 1: Orbital geometry of lunar satellite

$J_2 = 2.0323 \times 10^{-4}$, $J_3 = -8.4593 \times 10^{-6}$, $J_4 = 9.70434 \times 10^{-6}$, $J_5 = -7.42212 \times 10^{-7}$,
$J_6 = 1.37675 \times 10^{-5}, J_{22} = 2.2381 \times 10^{-5}, J_{31} = 2.8481 \times 10^{-5}, J_{32} = 4.8405 \times 10^{-6}$,
$J_{33} = 1.7117 \times 10^{-6}$, $R_M = 1738.1$km

2.1 Delaunay canonical-variables representation

To utilize the method of Lie transform, the Hamiltonian of the problem can be written in a canonical set, namely the Delaunay action-angle canonical set (L, G, H, l, g, h), defined as:

$$L = \sqrt{\mu a}, \quad G = \sqrt{\mu a(1-e^2)}, \quad H = \sqrt{\mu a(1-e^2)}\cos I,$$
$$l = M, \quad g = \omega, \quad h = \Omega - \lambda_m t.$$

2.2 Assessment of order of magnitudes

Consider that the most familiar orbits around the Moon come with semimajor axes ranging from about 1800 km to 2600 km (this will be our investigated domain of study), then the characteristic time and length (adopting an orbit radius of 2200 km as an average one). In this light, the nondimensional mean motion of the Moon n_m is considered to be of order 1. It can serve as a small parameter of the problem. The orders of magnitude $\mathcal{O}(x)$ of the perturbing terms can be constructed as follows:

$$\left|(n_m)^{x+\frac{1}{2}}\right| \leq \left|J_{n,m}\right| \equiv \mathcal{O}(x) \leq \left|(n_m)^{x-\frac{1}{2}}\right|$$

According to this formula, the following terms J_2, J_{22}, J_{31} , in addition to the term factored by the mean motion of the Moon, were considered of order 1 while the remaining terms, namely $J_3, J_4, J_5, J_6, J_{32}, J_{33}$ will be assumed of order 2.

Then equation (1) can now be written as

$$\mathcal{H} = \mathcal{H}_0 + n_m\mathcal{H}_1 + \frac{{n_m}^2}{2!}\mathcal{H}_2 \tag{3}$$

Where $\mathcal{H}_0$ is the Keplerian integrable part of the Hamiltonian, n_m is the nondimensional mean motion of the Moon, and it will be considered as a convenient small parameter of the problem. The term $n_m H$ such that $n_m = \lambda_m t +$ constantis added to the Hamiltonian to recover the autonomous character of the phase space. Now, the Hamiltonian of the problem (3) can be written as

$$\mathcal{H}_0 = -\frac{\mu^2}{2L^2}$$

(4)$\mathcal{H}_1 = -H + \frac{A_{1,2}}{4L^6}\Psi^3\left[(3S^2-2) - 3S^2\cos F_{2,2,0}\right] + \frac{3A_{1,22}}{4L^6}\Psi^3[2S^2\cos F_{0,0,2} + (1-C)^2\cos F_{2,2,-2} + (1+C)^2\cos F_{2,2,2}]$

$$+\frac{3A_{1,31}}{16L^8}\Psi^4\Big[(-1-11C+5C^2+15C^3)\cos F_{1,1,1} + (-1+11C+5C^2-15C^3)\cos F_{1,1,-1}$$
$$+5(1+C-C^2-C^3)\cos F_{3,3,+1} + 5(1-C-C^2+C^3)\cos F_{3,3,-1}\Big]$$

(5)and

$$\mathcal{H}_2 = \frac{A_{2,3}}{8L^8}\Psi^4\left[(15S^3-12S)\sin F_{1,1,0} - 5S^3\sin F_{3,3,0}\right] + \frac{A_{2,4}}{64L^{10}}\Psi^5[(24-120S^2+105S^4)$$
$$+(120S^2-140S^4)\cos F_{2,2,0} + 35S^4\cos F_{4,4,0}] + \frac{A_{2,5}}{64L^{12}}\Psi^6\Big[(240S-840S^3+630S^5)$$
$$\times \sin F_{1,1,0} + (280S^3-315S^5)\sin F_{3,3,0} + 63S^5\sin F_{5,5,0}\Big]$$
$$+\frac{A_{2,6}}{512L^{14}}\Psi^7\Big[(-160+1680S^2-3780S^4+2310S^6) - 231S^6\cos F_{6,6,0} + (-1260S^4 +$$
$$1386S^6)\cos F_{4,4,0} + (-1680S^2+5040S^4-3465S^6)\cos F_{2,2,0}\Big] + \frac{15A_{2,32}}{16L^8}\Psi^4\left[(2-4C-7C^2+2C^3)\sin F_{1,1,2} + (2+4C-7C^2-3C^3)\sin F_{1,1,-2} + (2+4C+C^2-2C^3)\sin F_{3,3,2} + (2-4C+C^2+2C^3)\sin F_{3,3,-2}\right] + \frac{15A_{2,33}}{8L^8}\Psi^4\Big[3(-1-C+C^2+C^3)\cos F_{1,1,3} + 3(-1+C+C^2-C^3)\times\cos F_{1,1,-3} + (-1-3C-3C^2-C^3)\cos F_{3,3,3} + (-1+3C-3C^2+C^3)\cos F_{3,3,-3}\Big] \tag{6}$$

Where $\Psi = a/r$

and the zero-order parameters are $A_{k,nm} = \frac{k!\mu^{n+2}R_M^n J_{nm}}{n_M^k}$ (7)

3. Methodology (Lie transformation brief introductory)

The Lie canonical transformations are utilized to normalize the Hamiltonian of the problem. The Hamiltonian of the problem then became mathematically tractable. The Lie transformations are based on eliminating some or all the angular variables from the Hamiltonian. One transformation will be performed to remove the fast variable, the true anomaly, leaving the argument of periapsis, ω, without averaging because we aim to study the frozen orbits. $\dot{g} = \frac{\partial \mathcal{H}^*}{\partial G}$ and $\dot{G} = -\frac{\partial \mathcal{H}^*}{\partial g}$ should be computed and set to zero, which is the criteria for the frozen orbits, namely$\dot{g} = 0$ and $\dot{G} = 0$

$\mathcal{H}_0^* = \mathcal{H}_0$

$$\mathcal{H}_n^* = \tilde{\mathcal{H}}_n + (\mathcal{H}_0; W_n)$$

Where W_n called the generating functions of the Lie transformation.

$$\tilde{\mathcal{H}}_n = \mathcal{H}_n + \sum_{j=1}^{n-1} \{C_{j-1}^{n-1}(\mathcal{H}_{n-j}; W_j) + C_j^{n-1} G_j \mathcal{H}_{n-j}\}$$

Where C_{j-1}^{n-1} is the binomial coefficients, and $G_j = L_j - \sum_{m=0}^{j-2} C_m^{j-1} L_{m+1} G_{j-m-1}$. It is clear that G_j is a recursive formula of Lie derivative given by Poison bracket as$L_W \mathcal{H} = (\mathcal{H}, W)$.

Let l be the fast variable in $\mathcal{H}$. $\mathcal{H}_n^*$ is chosen to be the average of $\tilde{\mathcal{H}}_n$ over l, i.e.

$$\mathcal{H}_n^* = \left\langle \tilde{\mathcal{H}}_n \right\rangle_\sigma, \sigma \equiv M, \Omega$$

So that the average $\langle . \rangle_\sigma$ of any general function $F(\sigma)$ is defined as ;

$$\langle F(\sigma) \rangle_\sigma = \frac{1}{2\pi} \int_0^{2\pi} F(\sigma) d\sigma$$

The short periodic part will be;

$$W_n = \left(\frac{\partial \mathcal{H}_0}{\partial L}\right)^{-1} \int (W_n; \mathcal{H}_0) d\sigma$$

The details at order one

$$\tilde{\mathcal{H}}_1 = \mathcal{H}_1$$

$$\mathcal{H}_1^* = \tilde{\mathcal{H}}_1 + (\mathcal{H}_0; W_1)$$

Choosing $\mathcal{H}_1^* = \left\langle \tilde{\mathcal{H}}_1 \right\rangle_\sigma$, then W_1 is therefore obtained by the quadrature

$$W_1 = \left(\frac{\partial \mathcal{H}_0}{\partial L}\right)^{-1} \int (W_1; \mathcal{H}_0) d\sigma$$

For more details on the procedure, see Deprit [39] and Kamel [40] and the reference therein. The averaging process over the fast variable, the true anomaly is computed in the next section.

4. Transformations of short periodic variables

Using the Lie canonical transformations method, Deprit [39], Kamel [40], Abd El-Salam, et al. [32], and Abd El-Salam, Ahmed [33], A number of normalizations can be performed to remove all the periodic coordinates from the Hamiltonian of the problem, firstly by removing the short cyclic terms, the true anomaly and retaining the first and second order secular and tesseral terms. Now, the newly transformed Hamiltonian $\mathcal{H}^*$ can be written as

$$\mathcal{H}^* = \mathcal{H}_0^* + n_m \mathcal{H}_1^* + \frac{{n_m}^2}{2} \mathcal{H}_2^* + \frac{{n_m}^2}{2} \mathcal{H}_{c22}^* \quad (8)$$

with

$$\mathcal{H}_0^* = \mathcal{H}_0|_{L=L'} = -\frac{\mu^2}{2L^2}$$

$$\mathcal{H}_1^* = A_{1,n}H + \frac{A_{1,2}}{4G^3L^3}(1-3C^2) + \frac{3A_{1,22}}{2}(1-C^2)\frac{1}{G^3L^3}\cos F_{0,0,2} + \frac{3A_{1,31}}{16}\Big[(-1+11C + +5C^2 -15C^3)\frac{e}{G^5L^3}\cos F_{0,1,-1} + (-1-11C+5C^2+15C^3)\frac{e}{G^5L^3}\cos F_{0,1,1}\Big] \quad (8.1)$$

$$\mathcal{H}_2^* = \frac{3A_{2,3}}{128}(16-88C^2+38C^4+9C^6)\frac{e}{G^5L^3}\sin F_{0,1,0} + \frac{3A_{2,4}}{128}\Big[(3-30C^2+35C^4)\frac{2+3e^2}{G^7L^3} - (1-8C^2+7C^4)\frac{e^2}{G^7L^3}\cos F_{0,2,0}\Big] + \frac{15A_{2,5}}{512}\Big[(8-116C^2+223C^4-70C^6)\frac{4e+3e^3}{G^9L^3}\sin F_{0,1,0} - \frac{7}{12}(8-26C^6+111C^4 -84C^2)\frac{e^3}{G^9L^3}\sin F_{0,3,0}\Big] + \frac{5A_{2,6}}{2048}\Big\{\Big[(5-105C^2+315C^4 - 231C^6)\frac{8+40e^2+15e^4}{G^{11}L^3} -105(1-19C^2+51C^4-33C^6)\frac{2e^2+e^4}{G^{11}L^3}\cos F_{0,2,0}\Big] + \frac{35}{2}(1-13C^2+23C^4 - 11C^6)\frac{e^4}{G^{11}L^3}\cos F_{0,4,0}\Big\} + \frac{15A_{2,32}}{16}[(2-4C - 7C^2+2C^3)\frac{e}{G^5L^3}\sin F_{0,1,2} + (2+4C-7C^2-2C^3)\frac{e}{G^5L^3}\sin F_{0,1,-2}\Big] + \frac{45A_{2,33}}{8}\Big[(-1+C+C^2-C^3)\frac{e}{G^5L^3}\cos F_{0,1,-3} + (-1-C+C^2+C^3)\frac{e}{G^5L^3}\cos F_{0,1,3}\Big] \quad (8.2)$$

$$\mathcal{H}_{c22}^* = \frac{3A_{1,2}^2}{32\mu^2}\Big[(-35C^4-5C^2+5)\frac{1}{L^3G^7} - (36C^4-24C^2+4)\frac{1}{L^4G^6} - (5C^4-18C^2 + 5)\frac{1}{L^5G^5}\Big] + (1-16C^2+15C^4)\Big[\frac{1}{L^5G^6} - \frac{1}{L^3G^8}\Big]\cos F_{0,2,0} \quad (8.3)$$

Where $\mathcal{H}_{c22}^*$, is the quadruple coupling term coming from the Poisson bracket of order two in the Lie procedure, including the Hamiltonian ($\mathcal{H}_1 + \mathcal{H}_1^*$) and the generating function W_1. In the subsequent sections 5, 6, and 7, the newly transformed Hamiltonian,$\mathcal{H}^*$ in (8.1), (8.2), and (8.3), will be utilized via the Hamilton canonical equations to calculate families of apsidal frozen line orbits revolving around the Moon.

5. The apsidal frozen line

Obtaining the frozen orbit by solving these two equations simultaneously

$$\dot{g} = \frac{\partial \mathcal{H}^*}{\partial G} = 0 \text{ and } \dot{G} = -\frac{\partial \mathcal{H}^*}{\partial g} = 0 \quad (9)$$

In our case, the equations can't be solved analytically to find the required families of frozen orbits at different altitudes with some range of small eccentricity, so we have to do some simplifications to make it possible to find families of frozen orbits. We find that if we take $g = 90°$or $270°$, the variation of the momentum with time equal to zero $\dot{G} = 0$ for all zonal potential terms and for most of the tesseral potential terms and the remaining terms of $\dot{G}$ almost equal to zero. By taking $h = 0°$or $180°$all the odd coefficient of the $\dot{G}$ will be vanished and the remaining terms can be solved in a semi-analytical form, then plotting the critical inclinations versus the eccentricity, the argument of periapsis, and the semi-major axis to find a family of frozen orbits.

The periapsis argument becomes frozen if $\frac{\partial \mathcal{H}^*}{\partial G} = 0$ (10)

$$\dot{g} = \alpha_0 + \alpha_1 \cos g + \alpha_2 \cos 2g + \alpha_4 \cos 4g + \beta_1 \sin g + \beta_2 \sin 2g + \beta_3 \sin 3g \quad (10.1)$$

$$\dot{G} = \bar{\alpha}_1 \cos g + \bar{\alpha}_2 \cos 2g + \bar{\alpha}_3 \cos 3g + \bar{\beta}_1 \sin g + \bar{\beta}_2 \sin 2g + \bar{\beta}_4 \sin 4g \quad (10.2)$$

Where α_0, α_1, α_2, α_4, $\bar{\alpha}_1$, $\bar{\alpha}_2$,$\bar{\alpha}_3$, β_1, β_2, β_3, $\bar{\beta}_1$, $\bar{\beta}_2$, and $\bar{\beta}_4$ are lengthy expressions in $(a, e, I,\text{and}\Omega)$ and available upon request.

6. Solution for the inclination

The solution of equation (10.1), for the inclination, $\dot{g}(I) = 0$ can be obtained as

$$\mathcal{A}_6 C^6 + \mathcal{A}_4 C^4 + \mathcal{A}_2 C^2 + \mathcal{A}_0 = 0 \qquad (11)$$

Equation (11) can be solved to give the critical inclinations ($C = cos\, I$) in only two real solutions as follows:

$$I_{1,2} = cos^{-1}\left(\pm\sqrt{-\frac{\mathcal{A}_4}{3\mathcal{A}_6} - \frac{2^{1/3}\mathcal{A}_2}{\mathcal{A}^*} + \frac{2^{1/3}\mathcal{A}_4^2}{3\mathcal{A}_6\mathcal{A}^*} + \frac{\mathcal{A}^*}{32^{1/3}\mathcal{A}_6}}\right) \qquad (12)$$

Where

$$\mathcal{A}^* = \sqrt[3]{-2\mathcal{A}_4^3 + 9\mathcal{A}_2\mathcal{A}_4\mathcal{A}_6 - 27\mathcal{A}_0\mathcal{A}_6^2 + \sqrt{4(-\mathcal{A}_4^2 + 3\mathcal{A}_2\mathcal{A}_6)^3 + (-2\mathcal{A}_4^3 + 9\mathcal{A}_2\mathcal{A}_4\mathcal{A}_6 - 27\mathcal{A}_0\mathcal{A}_6^2)^2}}$$

The included-lengthy coefficients $\mathcal{A}_0, \mathcal{A}_2, \mathcal{A}_4,\text{and}\mathcal{A}_6$ are lengthy expressions in $(a, e, I,\text{and}\Omega)$ and available upon request from the corresponding author.

7. Results and Discussion

7.1 Graphical representation of equation (12)

In what follows, A numerical simulation will be given for the fully considered perturbing model, i.e., there are three terms in order 1, in addition to six terms in order 2. We reproduce the following figures for representing the critical$I$versus a, see **Fig. 2,** and representing the critical$I$versus e, see **Fig. 3**. By putting the value of$g = 90.0^{\circ}$and$h = 0.0^{\circ}$or180° while $e \in [0.05,0.3]$ with stepsize $.05$, three groups of curves had been plotted.

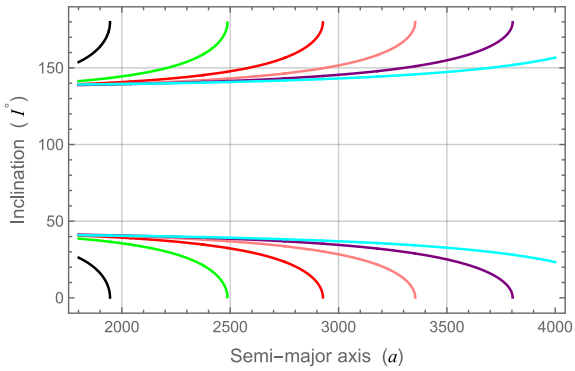

Figure. 2 Real roots of (11) vs. a.

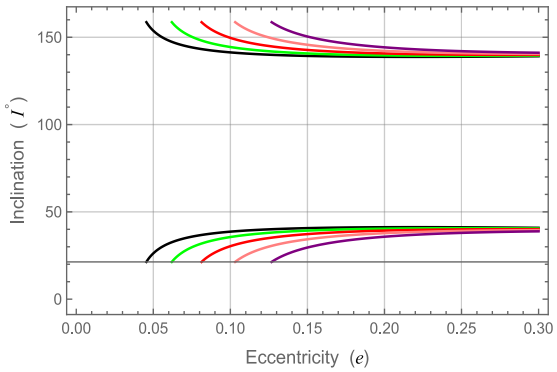

Figure. 3 Real roots of (11) vs. e.

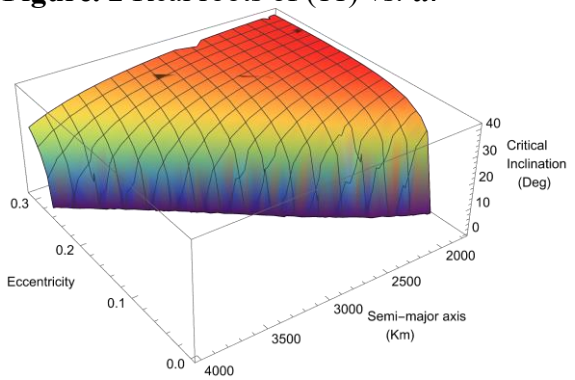

Figure. 4 3D representation of the 1st root of I vs. a and e.

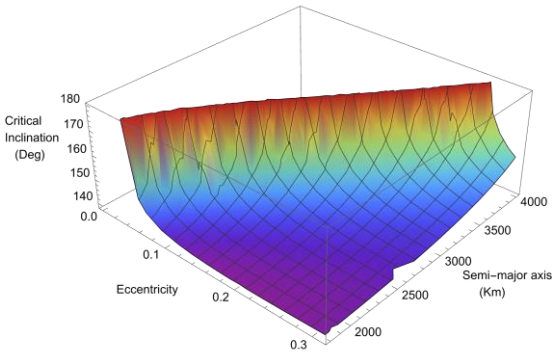

Figure. 5 3D representation of the 2nd root of I vs. a and e.

7.1.1 Discussion of Figures 2-5

The color code for the 2D figures is as follows: for the semimajor axes, black, green, red, pink, and purple curves had been plotted, which corresponded to1800,2000,2200,2400, and 2600km, respectively. While for the eccentricity, black, green, red, pink, purple, and cyan curves were plotted, which corresponded to $0.05 - 0.3$, respectively with a step size of $.05$. As we see from **Fig. 2**, there are two families of direct frozen orbits and retrograde frozen orbits. For the direct family, all roots have different eccentricities that guarantee $\dot{g} = 0$ having critical inclination $40° \pm 1°$ at low altitudes, then vanish at different altitudes from small eccentricity to high eccentricities, respectively. The same behavior for the retrograde family almost roots start with critical inclination $140° \pm 1°$ at low altitudes. From **Fig. 3**, there are no real roots near the domain of the circular orbits $e \in [0.0,0.04]$ and there is a family of frozen direct orbits having different critical inclinations at low eccentricities and approaching the same critical inclination $40° \pm 1°$ for different semi-major axes, while for the retrograde orbits, the different curves approach inclination $140° \pm 1°$. In **Figs. 4 and 5**, frozen orbits can be constructed based on some selected orbital elements.

Table 1: TheI_{c_1} and I_{c_2}, corresponding to different values of a, and e. Note that at $e = 0.0$ the critical inclinations $I_{1,2} = \emptyset$ along all values of the semi-major axis.

a \ e		0.05	0.10	0.15	0.20	0.25	0.30
1800 km	I_{c_1}	26.2511°	38.6636°	40.6795°	41.1992°	41.165°	40.86°
	I_{c_2}	153.749°	141.336°	139.321°	138.801°	138.835°	139.14°
2000	I_{c_1}	\	35.5866°	39.2695°	40.3758°	40.6418°	40.517°
	$\boldsymbol{I_{c_2}}$	\	144.413°	140.73°	139.624°	139.358°	139.483°
2200	I_{c_1}	\	30.3457°	37.266°	39.2763°	39.9648°	40.0811°
	I_{c_2}	\	149.654°	142.734°	140.724°	140.035°	139.919°
2400	I_{c_1}	\	18.9907°	34.3045°	37.7965°	39.0922°	39.5328°
	I_{c_2}	\	161.009°	145.696°	142.204°	140.908°	140.467°
2600	I_{c_1}	\	\	29.5712°	35.7633°	37.9644°	38.8467°
	I_{c_2}	\	\	150.429°	144.237°	142.036°	141.153°

In the second case: By using equation (11), we plot the following set of figures of Iversus a and e, putting the value of $g = 270.0°$and $h = 0.0°$or$180°$while $e \in [0.05,0.3]$ with stepsize 0.05, three groups of curves were plotted.

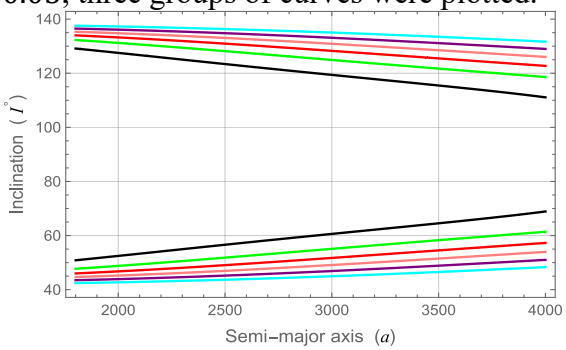

Figure. 6 . Real roots of (11) vs. a.

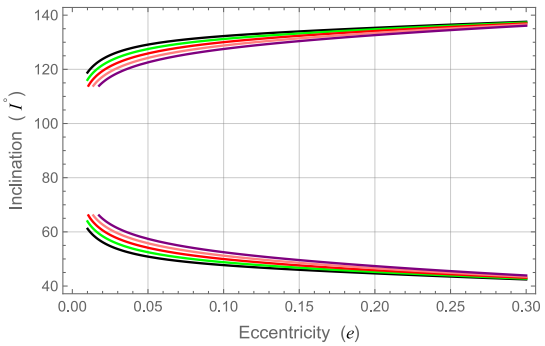

Figure. 7 . Real roots of (11) vs. e.

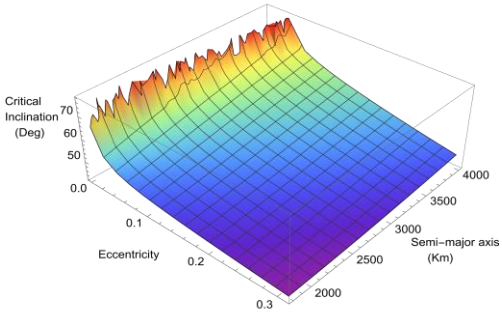

Figure. 8 3D representation of the 1st root of I vs. a and e.

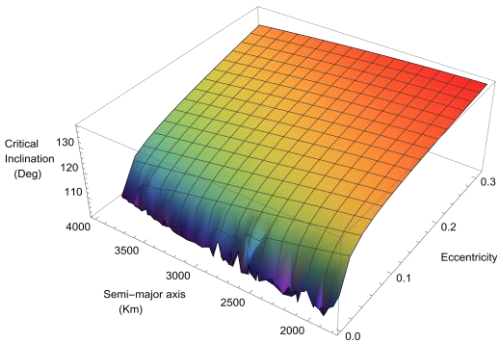

Figure. 9 3D representation of the 2nd root of I vs. a and e.

7.2.2 Discussion of Figures 6-9

We can easily see from **Fig. 6**, real roots along the semi-major axis that construct families of frozen orbits with different$e$come closer in the low altitude ranges from $I \simeq [45^\circ \pm 5^\circ]$ and diverse as the semi-major axis increases. The same behavior occurs for the retrograde orbits real roots come closer in the low altitudes ranges from $I \simeq [135^\circ \pm 5^\circ]$. From **Fig. 7**, it's clear that we have continuous roots of frozen orbits at both direct and retrograde orbits for different semi-major axes. It's obvious that near-circular orbits have a difference in the critical inclinations between the different semi-major axes while that difference in critical inclinations vanishes at higher eccentricities. In **Figs. 8 and 9**, the real roots extend along the semi-major axis and along the eccentricity axis except in near-circular orbits.

Table 2: The I_{c_1} and I_{c_2}, corresponding to different values of a and e. Note that at $e = 0$ the critical $I_1 \simeq 71.47^\circ$and$I_2 \simeq 108.53^\circ$ along all values of$a$.

a \ e		0.05	0.10	0.15	0.20	0.25	0.30
1800 km	I_{c_1}	50.8651°	47.7235°	46.0032°	44.6712°	43.5029°	42.4372°
	I_{c_2}	129.135°	132.276°	133.997°	135.329°	136.497°	137.563°
2000	I_{c_1}	52.4805°	48.7991°	46.7651°	45.2219°	43.9005°	42.7204°
	$\boldsymbol{I_{c_2}}$	127.52°	131.201°	133.235°	134.778°	136.099°	137.28°
2200	I_{c_1}	54.1337°	49.9706°	47.6258°	45.8595°	44.3691°	43.0587°
	I_{c_2}	125.866°	130.029°	132.374°	134.14°	135.631°	136.941°
2400	I_{c_1}	55.7894°	51.2096°	48.5701°	46.5775°	44.9071°	43.4529°
	I_{c_2}	124.211°	128.79°	131.43°	133.423°	135.093°	136.547°
2600	I_{c_1}	57.4257°	52.4901°	49.5809°	47.3667°	45.5108°	43.9026°
	I_{c_2}	122.574°	127.51°	130.419°	132.633°	134.489°	136.097°

7.2 Three-dimensional representation of g full range

In this section, a new set of figures will be plotted for the critical I versus the full range of g, the investigated ranges of e and a. Using $h = 0^\circ$or180°, $g = 90^\circ$for the left-column figures and $g = 270^\circ$for the right-column figures. It's clear that the surface of $\dot{g} = 0$ and the surface of $\dot{G} = 0$ are intersected in all figures that reflect the existence of frozen orbits along the line of intersection.

The color code for 3D figures is as follows: $\dot{g}$ take the new yellow color while the blue color for $\dot{G}$

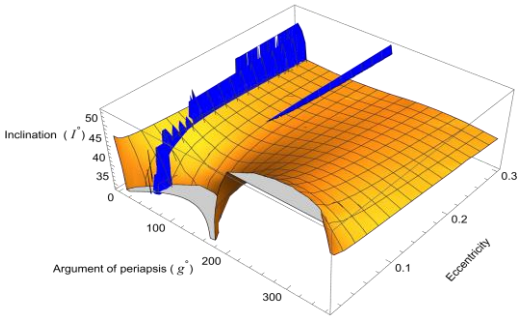

Figure. 10 3D plot of the inclination 1st root of $\dot{g}$ Vs. $\dot{G}$ with $a = 1800$km

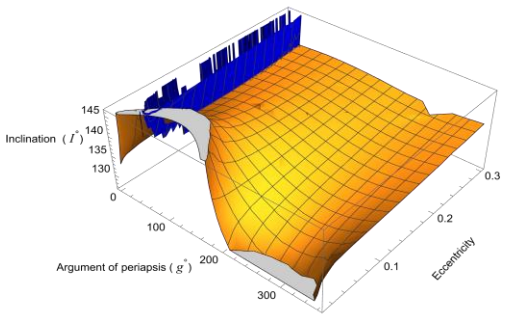

Figure. 11 3D plot of the inclination 2nd root of $\dot{g}$ Vs. $\dot{G}$ with $a = 1800$km

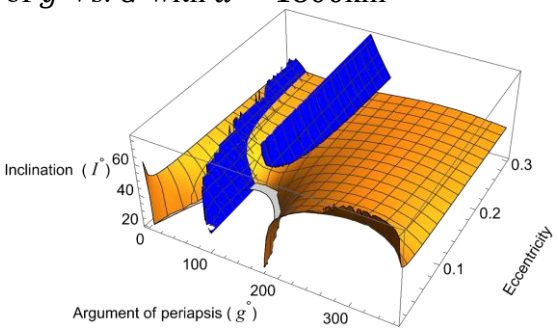

Figure. 12 3D plot of the inclination 1st root of $\dot{g}$ Vs. $\dot{G}$ with $a = 2600$km

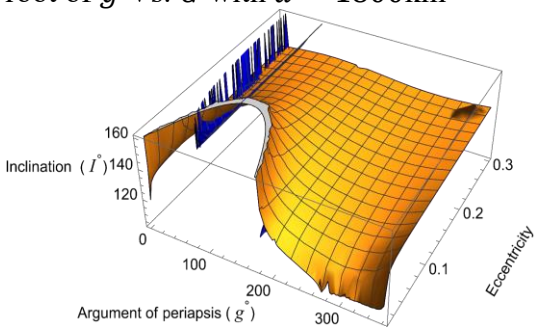

Figure. 13 3D plot of the inclination 2nd root of $\dot{g}$ Vs. $\dot{G}$ with $a = 2600$km

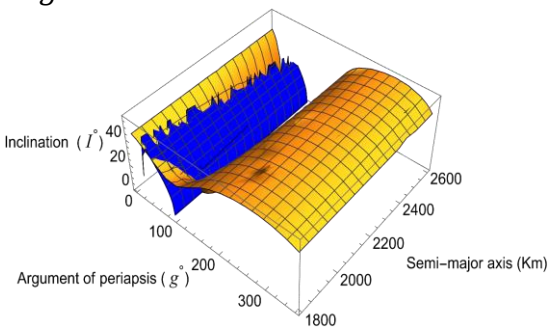

Figure. 14 3D plot of the inclination 1st root of $\dot{g}$ Vs. $\dot{G}$ with $e = 0.05$

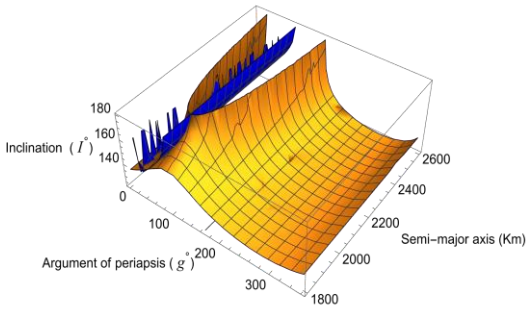

Figure. 15 3D plot of the inclination 2nd root of $\dot{g}$ Vs. $\dot{G}$ with $e = 0.05$

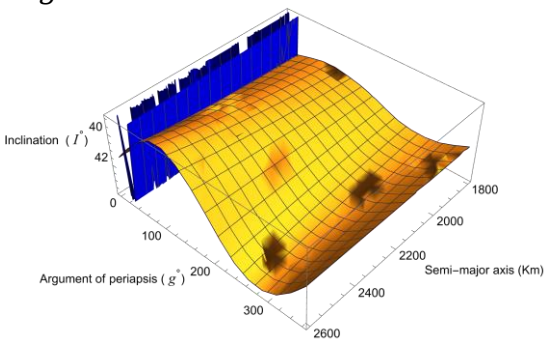

Figure. 16 3D plot of the inclination 1st root of $\dot{g}$ Vs. $\dot{G}$ with $e = 0.3$

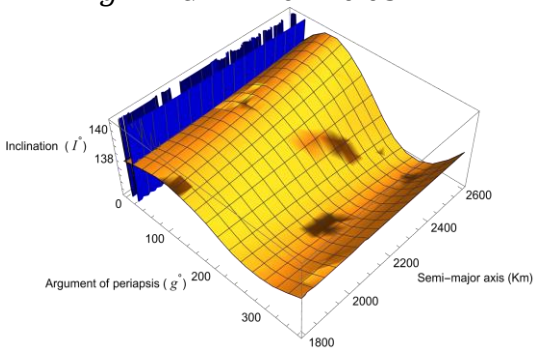

Figure. 17 3D plot of the inclination 2nd root of $\dot{g}$ Vs. $\dot{G}$ with $e = 0.3$

7.3 Numerical solution of the frozen orbits

In this section, a new set of figures will be plotted for the critical I versus a and put the value of $g = 90.0^\circ$ for the left column, $g = 270.0^\circ$ for the right column, and $h = 90^\circ$ or 270° while $e \in [0.05, 0.3]$ with step size $.05$ and two groups of curves can be plotted and a set of figures for the critical I versus e with the same conditions.

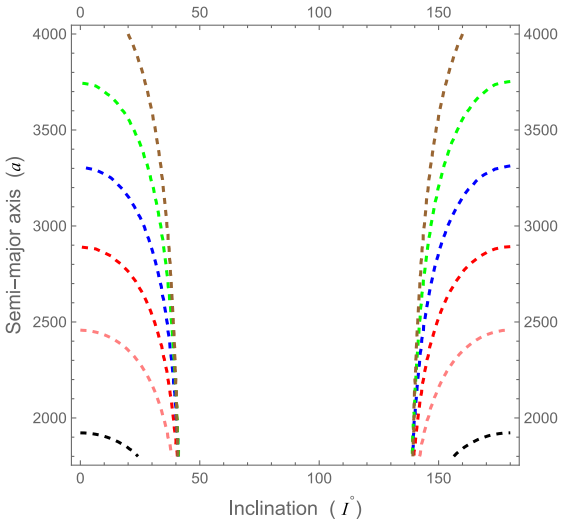

Figure. 18 The contour plot of the *I* vs. *a*.

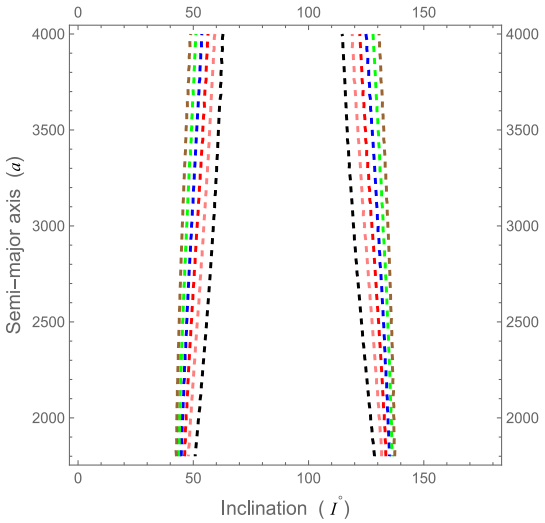

Figure. 19 The contour plot of the *I* vs. *a*.

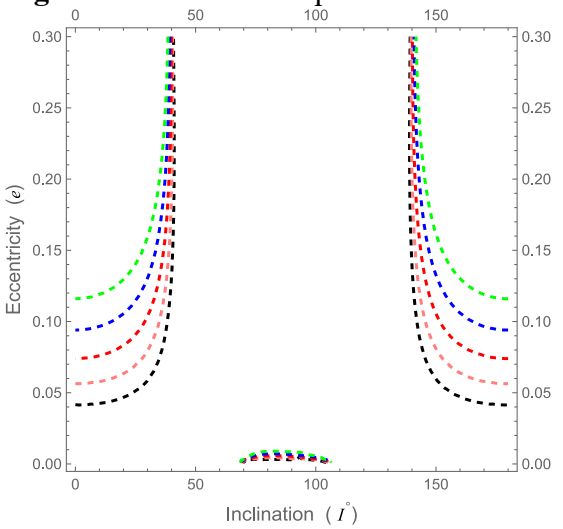

Figure. 20 The contour plot of the *I* vs. *e*.

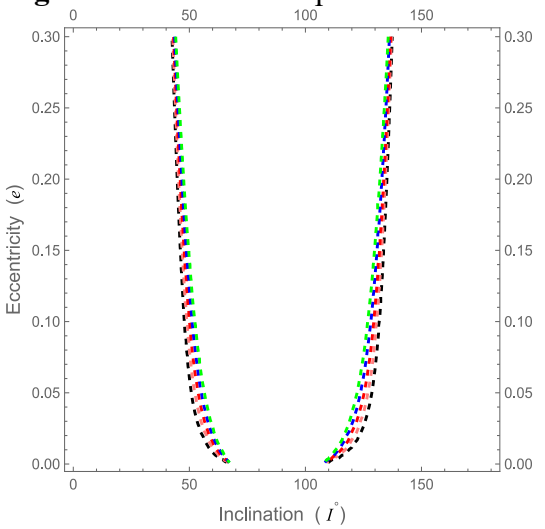

Figure. 21 The contour plot of the *I* vs. *e*.

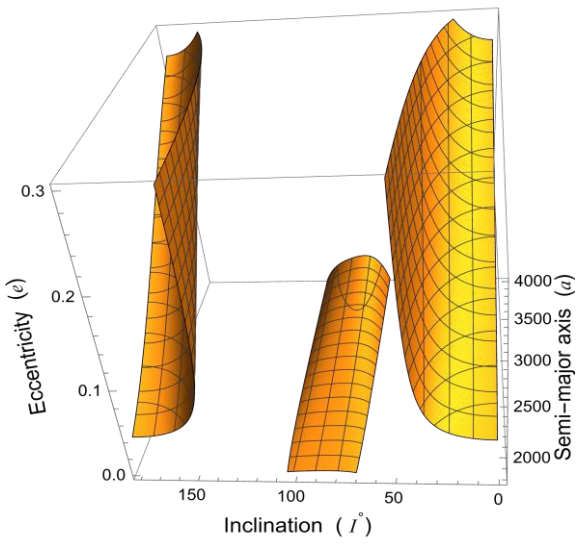

Figure. 22 3D contour plot of the *I* vs. *e*.

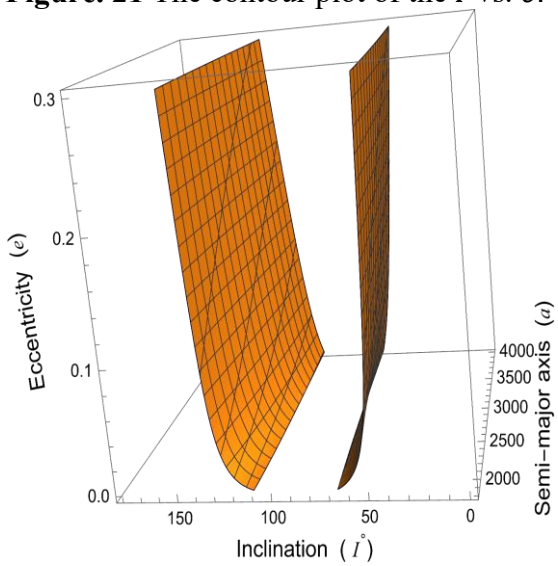

Figure. 23 3D contour plot of the *I* vs. *e*.

7.3.1 Discussion of Figures 18-23

The color code for the 2D figures is as follows: for the semimajor axes, black, orange, red, blue, and green curves were plotted that corresponded to $1800,2000,2200,2400$and 2600km, respectively. As for the eccentricity, black, orange, red, blue, green, and brown curves were plotted that corresponded to $0.05-0.3$, respectively with a step size of $.05$.
We can find in **Fig. 18** a family of frozen direct orbits for different eccentricities, and as the orbit becomes more elliptic, the range of the semi-major axis extends for the available frozen orbits. Frozen orbits can be constructed with critical inclination $I \simeq 40°$at low altitudes $a <$ 2000kmthen reduce at high semi-major axis. The same behavior is observed for the retrograde orbits; most orbits with different eccentricities have nearly the same critical inclination $I \simeq 140°$. In **Fig. 19**, There are families of frozen direct orbits that can be seen along all semi-major axes around the critical inclination $I \in [40°, 50°]$ at low altitudes and reach $I \in [50°, 62°]$ at the semi-major axis $a = 4000$km. The same is true for the retrograde orbits but with different values of I.

Table 3: The I_{c_1} and I_{c_2}, correspond to different values of a, e. where $g = 90°$.

a \ e		0.05	0.10	0.15	0.20	0.25	0.30
1800 km	I_{c_1}	24.1478°	38.251°	40.4618°	41.0479°	41.0473°	40.7641°
	I_{c_2}	156.354°	142.068°	139.735°	139.084°	139.044°	139.301°
2000	I_{c_1}	\	34.8326°	38.9196°	40.1476°	40.4707°	40.386°
	$\boldsymbol{I_{c_2}}$	\	145.589°	141.348°	140.032°	139.654°	139.708°
2200	I_{c_1}	\	28.8807°	36.6996°	38.9353°	39.7203°	39.8915°
	I_{c_2}	\	151.609°	143.648°	141.301°	140.445°	140.225°
2400	I_{c_1}	\	15.2216°	33.367°	37.2867°	38.7464°	39.2734°
	I_{c_2}	\	165.06°	147.056°	143.013°	141.465°	140.877°
2600	I_{c_1}	\	\	27.9399°	34.9949°	37.4774°	38.4956°
	I_{c_2}	\	\	152.512°	145.368°	142.785°	141.692°

Table 4: The I_{c_1} and I_{c_2}, correspond to differnet values of a, e. where $g = 270°$.

a \ e		0.05	0.10	0.15	0.20	0.25	0.30
1800 km	I_{c_1}	50.8023°	47.7928°	46.0926°	44.7629°	43.5907°	42.5177°
	I_{c_2}	128.621°	131.907°	133.716°	135.106°	136.316°	137.416°
2000	I_{c_1}	52.2826°	48.8491°	46.8655°	45.3358°	44.0144°	42.8272°
	$\boldsymbol{I_{c_2}}$	126.967°	130.749°	132.875°	134.485°	135.858°	137.082°
2200	I_{c_1}	53.736°	49.9756°	47.7271°	45.993°	44.5104°	43.1951°
	I_{c_2}	125.325°	129.505°	131.932°	133.769°	135.32°	136.683°
2400	I_{c_1}	55.1212°	51.1378°	48.6573°	46.7249°	45.0754°	43.6214°
	I_{c_2}	123.741°	128.211°	130.908°	132.969°	134.704°	136.22°
2600	I_{c_1}	56.4127°	52.3043°	49.6346°	47.5192°	45.7037°	44.1045°
	I_{c_2}	122.245°	126.901°	129.825°	132.095°	134.017°	135.693°

8. Conclusion

Finally, a first normalized Hamiltonian of the problem of a lunar orbiter truncating the lunar potential beyond the sixth zonal harmonic coefficients, in addition to the largest tesseral and sectoral Harmonics is obtained after that analytical solutions and graphical representations. Here we rewrite in simple form the main points concluded thoroughout the paper:

1. In the full model representations, i.e., considering the perturbations at order 1 in addition to order 2, different families of direct frozen and retrograde frozen orbits had been obtained in terms of the eccentricity and semi-major axis via solving $\dot{g}$ equation at specific values of g and h to guarantee minimizing the $\dot{G}$ equation.
2. I section 7.2, a new set of figures had been represented frozen orbits, the critical I versus the full range of g by using $h = 0°$or$180°$, $g = 90°$ and $g = 270°$. It's clear that the surface of $\dot{g} = 0$and the surface of $\dot{G} = 0$ are intersected in all figures that reflect the existence of frozen orbits along the line of intersection.
3. In section 7.3, choosing$g = 90°$and $h = 90°$or$270°$to guarantee $\dot{G} = 0$ and obtain a numerical representation of the full $\dot{g}$ equation which constructs families of frozen orbits in the polar regions, plus families of frozen orbits in the direct and retrograde orbits.

Conflict of interest

All authors declare that they have no conflicts of interest.

Data Availability Statement

No data is associated with the manuscript.

References

[1] Weilian, Y. (2002). A First Order Solution for Frozen Orbit. Chinese Space Science and Technology, 22(04)..

[2] Brouwer, D. (1959). Solution of the problem of artificial satellite theory without drag. The Astronomical Journal, 64, 378. https://ui.adsabs.harvard.edu/link_gateway/1959AJ.....64..378B/doi:10.1086/107958

[3] Hori, G. I. (1960). The motion of an artificial satellite in the vicinity of the critical inclination. Astronomical Journal, Vol. 65, p. 291 (1960), 65, 291. https://ui.adsabs.harvard.edu/link_gateway/1960AJ.....65..291H/doi:10.1086/108248

[4] Garfinkel, B. (1960). On the motion of a satellite in the vicinity of the critical inclination. Astronomical Journal, Vol. 65, p. 624 (1960), 65, 624. https://ui.adsabs.harvard.edu/link_gateway/1960AJ.....65..624G/doi:10.1086/108308

[5] Izsak, I. G. (1962). On the critical inclination in satellite theory. SAO Special Report# 90 (1962), 90. https://ui.adsabs.harvard.edu/abs/1962SAOSR..90.....I/abstract

[6] Aoki, S. (1963). A Contribution to the Theory of Critical Inclination of Close Earth Satellites. National Aeronautics and Space Administration. https://ui.adsabs.harvard.edu/link_gateway/1962AJ.....67S.571A/doi:10.1086/108656

[7] Hoots, F. R., & Fitzpatrick, P. M. (1979). The rotational motion of an earth orbiting gyroscope according to the Einstein theory of general relativity. Celestial mechanics, 20(1), 19-42. https://doi.org/10.1007/BF01236606

[8] Delhaise, F., & Henrard, J. (1993). The problem of critical inclination combined with a resonance in mean motion in artificial satellite theory. Celestial Mechanics and Dynamical Astronomy, 55, 261-280. https://doi.org/10.1007/BF00692514

[9] Henrard, J. (1990). A semi-numerical perturbation method for separable Hamiltonian systems. Celestial Mechanics and Dynamical Astronomy, 49, 43-67. https://doi.org/10.1007/BF00048581

[10] Delhaise, F., & Morbidelli, A. (1993). Luni-solar effects of geosynchronous orbits at the critical inclination. Celestial Mechanics and Dynamical Astronomy, 57, 155-173. https://doi.org/10.1007/BF00692471

[11] Delsate, N., Robutel, P., Lemaître, A., & Carletti, T. (2010). Frozen orbits at high eccentricity and inclination: application to Mercury orbiter. Celestial Mechanics and Dynamical Astronomy, 108, 275-300. https://doi.org/10.1007/s10569-010-9306-2

[12] Park, S. Y., & Junkins, J. (1994). Orbital mission analysis for a lunar mapping satellite. In Astrodynamics Conference (p. 3717). https://doi.org/10.2514/6.1994-3717

[13] Scheeres, D. J., Guman, M. D., & Villac, B. F. (2001). Stability analysis of planetary satellite orbiters: application to the Europa orbiter. Journal of Guidance, Control, and Dynamics, 24(4), 778-787. https://doi.org/10.2514/2.4778

[14] San-Juan, J. F., Lara, M., & Ferrer, S. (2006). Phase space structure around oblate planetary satellites. Journal of guidance, control, and dynamics, 29(1), 113-120. https://doi.org/10.2514/1.13385

[15] Paskowitz, M. E., & Scheeres, D. J. (2006). Design of science orbits about planetary satellites: application to Europa. Journal of Guidance, Control, and Dynamics, 29(5), 1147-1158. https://doi.org/10.2514/1.19464

[16] Lara, M., Palacián, J. F., Yanguas, P., & Corral, C. (2010). Analytical theory for spacecraft motion about Mercury. Acta Astronautica, 66(7-8), 1022-1038. https://doi.org/10.1016/j.actaastro.2009.10.011

[17] Lara, M., San-Juan, J. F., & López-Ochoa, L. M. (2013). Precise Analytical Computation of Frozen-Eccentricity, Low Earth Orbits in a Tesseral Potential. *Mathematical Problems in Engineering*, *2013*(1), 191384 https://doi.org/10.1155/2013/191384

[18] Lara, M., Palacián, J. F., & Russell, R. P. (2010). Mission design through averaging of perturbed

Keplerian systems: the paradigm of an Enceladus orbiter. Celestial Mechanics and Dynamical Astronomy, 108, 1-22. https://doi.org/10.1007/s10569-010-9286-2

[19] Tzirti, S., Tsiganis, K., & Varvoglis, H. (2009). Quasi-critical orbits for artificial lunar satellites. Celestial Mechanics and Dynamical Astronomy, 104, 227-239. https://doi.org/10.1007/s10569-009-9207-4

[20] Tzirti, S., Tsiganis, K., & Varvoglis, H. (2010). Effect of 3rd-degree gravity harmonics and Earth perturbations on lunar artificial satellite orbits. Celestial Mechanics and Dynamical Astronomy, 108, 389-404. https://doi.org/10.1007/s10569-

[21] Liu, X., Baoyin, H., & Ma, X. (2010). Five special types of orbits around Mars. Journal of guidance, control, and dynamics, 33(4), 1294-1301. https://doi.org/10.2514/1.48706

[22] Liu, X., Baoyin, H., & Ma, X. (2011). Analytical investigations of quasi-circular frozen orbits in the Martian gravity field. Celestial Mechanics and Dynamical Astronomy, 109, 303-320. https://doi.org/10.1007/s10569-010-9330-2

[23] Carvalho, J. D. S., Vilhena de Moraes, R., & Prado, A. F. B. A. (2010). Some orbital characteristics of lunar artificial satellites. Celestial Mechanics and Dynamical Astronomy, 108, 371-388. https://doi.org/10.1007/s10569-010-9310-6

[24] Carvalho, J. P. S., Mourao, D. C., Elipe, A., De Moraes, R. V., & Prado, A. F. B. A. (2012). Frozen orbits around Europa. International Journal of Bifurcation and Chaos, 22(10), 1250240. https://doi.org/10.1142/S0218127412502409

[25] Ulivieri, C., Circi, C., Ortore, E., Bunkheila, F., & Todino, F. (2013). Frozen orbital plane solutions for satellites in nearly circular orbit. Journal of Guidance, Control, and Dynamics, 36(4), 935-945. https://doi.org/10.2514/1.59734

[26] Pardal, P. C. P. M., de Moraes, R. V., & Kuga, H. K. (2014). Effects of geopotential and atmospheric drag effects on frozen orbits using nonsingular variables. Mathematical Problems in Engineering, 2014. https://doi.org/10.1155/2014/678015

[27] Rahoma, W. A., & Abd El-Salam, F. A. (2014). The effects of Moon's uneven mass distribution on the critical inclinations of a lunar orbiter. Journal of Astronomy and Space Sciences, 31(4), 285-294. https://doi.org/10.5140/JASS.2014.31.4.285

[28] Rahoma, W. A., Khattab, E. H., & Abd El-Salam, F. A. (2014). Relativistic and the first sectorial harmonics corrections in the critical inclination. Astrophysics and Space Science, 351, 113-117. https://doi.org/10.1007/s10509-014-1811-4

[29] Zotos, E. E. (2015). Classifying orbits in the restricted three-body problem. Nonlinear Dynamics, 82, 1233-1250. https://doi.org/10.1007/s11071-015-2229-4

[30] Haberman, R., Rand, R., & Yuster, T. (1999). Resonant capture and separatrix crossing in dual-spin spacecraft. Nonlinear Dynamics, 18, 159-184. https://doi.org/10.1023/A:1008393913849

[31] Quinn, D., Rand, R., & Bridge, J. (1995). The dynamics of resonant capture. advances in nonlinear dynamics: methods and applications, 1-20. https://doi.org/10.1007/978-94-011-0367-1_1

[32] Abd El-Salam, F. A., Ahmed, M. K., & Radwan, M. (2005). The post-Newtonian effects in the critical inclination problem in artificial satellite theory. Applied mathematics and computation, 161(3), 813-823. https://doi.org/10.1016/j.amc.2003.12.041

[33] Abd El-Salam, F. A., & Ahmed, M. K. (2005). Canonical solution of the critical inclination problem taking into account PN-corrections. Applied mathematics and computation, 161(3), 825-841. https://doi.org/10.1016/j.amc.2003.12.042

[34] Khattab, E. H., Radwan, M., & Rahoma, W. A. (2020). Frozen orbits construction for a lunar solar sail. Journal of Astronomy and Space Sciences, 37(1), 1-9. https://doi.org/10.5140/JASS.2020.37.1.1

[35] Sirwah, M. A., Tarek, D., Radwan, M., & Ibrahim, A. H. (2020). A study of the moderate altitude frozen orbits around the Moon. Results in Physics, 17, 103148. https://doi.org/10.1016/j.rinp.2020.103148

[36] Abd El-Salam, F. A., Alamri, S. Z., Abd El-Bar, S. E., & Seadawy, A. R. (2018). Frozen apsidal line orbits around triaxial Moon with coupling quadrupole nonlinearity. Results in Physics, 10, 176-186. https://doi.org/10.1016/j.rinp.2018.05.029

[37] Abd El-Salam, F. A., Rahoma, W. A., El-Saftawy, M. I., & Mostafa, A. (2023). The frozen orbits of the charged satellites under zonal harmonics perturbation. Advances in Space Research, 71(11), 4787-4801. https://doi.org/10.1016/j.asr.2023.01.040

[38] Lara, M. (2008). Simplified Equations for Computing Science Orbits Around Planetary Satellites, Journal of guidance, control and dynamics. Vol. 31, No. 1, January–February 2008. https://doi.org/10.2514/1.31107

[39] Deprit, A., (1969). "Canonical transformations depending on a small parameter". Celest. Mech. 1,12:30. DOI: https://doi.org/10.1007/ BF01230629.

[40] Kamel, A.A., (1970). "Perturbation method in the theory of nonlinear oscillations". Celest. Mech. 3, 90:106. DOI: https://doi.org/10.1007/ BF01230435.